Vertical-Mode and Cloud Decomposition of Large-Scale Convectively Coupled Gravity Waves in a Two-Dimensional Cloud-Resolving Model

STEFAN N. TULICH
CIRES/NOAA/Earth System Research Laboratory, Boulder, Colorado

DAVID A. RANDALL
Department of Atmospheric Science, Colorado State University, Fort Collins, Colorado

BRIAN E. MAPES
Rosenstiel School of Marine and Atmospheric Science, University of Miami, Miami, Florida

(Manuscript received 9 December 2005, in final form 31 May 2006)

ABSTRACT

This paper describes an analysis of large-scale [O(1000 km)] convectively coupled gravity waves simulated using a two-dimensional cloud-resolving model. The waves develop spontaneously under uniform radiative cooling and approximately zero-mean-flow conditions, with wavenumber 2 of the domain appearing most prominently and right-moving components dominating over left-moving components for random reasons. The analysis discretizes the model output in two ways. First, a vertical-mode transform projects profiles of winds, temperature, and heating onto the vertical modes of the model's base-state atmosphere. Second, a cloud-partitioning algorithm sorts sufficiently cloudy grid columns into three categories: shallow convective, deep convective, and stratiform anvil.

Results show that much of the tilted structures of the waves can be captured by just two main vertical spectral "bands," each consisting of a pair of vertical modes. The "slow" modes have propagation speeds of 16 and 18 m s^{-1} (and roughly a full-wavelength vertical structure through the troposphere), while the "fast" modes have speeds of 35 and 45 m s^{-1} (and roughly a half-wavelength structure). Deep convection anomalies in the waves are more or less in phase with the low-level cold temperature anomalies of the slow modes and in quadrature with those of the fast modes. Owing to the characteristic life cycle of deep convective cloud systems, shallow convective heating peaks ~2 h prior to maximum deep convective heating, while stratiform heating peaks ~3 h after. The onset of deep convection in the waves is preceded by a gradual deepening of shallow convection lasting a period of many hours.

Results of this study are in broad agreement with simple two-mode models of unstable large-scale wave growth, under the name "stratiform instability." Differences here are that 1) the key dynamical modes have speeds in the range 16–18 m s^{-1}, rather than 23–25 m s^{-1} (owing to a shallower depth of imposed radiative cooling), and 2) deep convective heating, as well as stratiform heating, is essential for the generation and maintenance of the slow modes.

1. Introduction

Convectively coupled equatorial waves are a well-documented class of tropical weather phenomena (Takayabu 1994; Wheeler and Kiladis 1999; Straub and Kiladis 2002; Yang et al. 2003; Roundy and Frank 2004). They are large-scale [O(1000 km)] zonally propagating cloud disturbances that have dispersion properties and horizontal dynamical structures similar to those of shallow-water equatorial modes, with implied equivalent depths in the range 12–50 m (corresponding to Kelvin/gravity wave speeds in the range 11–22 m s^{-1}). Such organized cloud systems constitute an important predictable part of subseasonal tropical weather (Wheeler and Weickmann 2001). Hence, it is of both practical and scientific interest to understand the mechanisms responsible for their generation and maintenance, as well as the dynamics that govern their behavior.

Several types of mechanistic models have been advanced as theories of convectively coupled tropical

Corresponding author address: Dr. Stefan N. Tulich, CIRES/NOAA/Earth System Research Laboratory, University of Colorado, 216 UCB, Boulder, CO 80309-0216.
E-mail: stefan.tulich@noaa.gov

DOI: 10.1175/JAS3884.1

waves. The simplest involve a single cloud type, deep convective, interacting with a single dynamical mode of vertical structure, corresponding to the first baroclinic mode of the troposphere (e.g., Goswami and Goswami 1991; Emanuel et al. 1994; Yano et al. 1995; Lin and Neelin 2002). Slightly more complex models involve two or three basic cloud types (including shallow convective, deep convective, and stratiform anvil) interacting with two vertical modes: a shallow (second baroclinic) mode and a deeper (first baroclinic) mode (e.g., Mapes 2000; Majda and Shefter 2001; Wu 2003; Haertel and Kiladis 2004; Khouider and Majda 2006). Both model types are able to produce waves whose periods and zonal wavelengths broadly match those of observed tropical waves. Models with two vertical modes can also produce waves with crudely realistic vertical structures.

Judging from these results, it would seem that models with crude vertical resolution are indeed useful for studying the coupling between tropical waves and convection. Nevertheless, a limitation of such models, as well as more sophisticated models with finer vertical resolution (e.g., Hayashi 1970; Stark 1976; Davies 1979; Crum and Stevens 1983; Chang and Lim 1988; Chao and Lin 1994; Su et al. 2000; Lindzen 2003), is that their predictions depend heavily on uncertain closure assumptions. Also, the vertical distributions of temperature and moisture tendencies due to unresolved cloud processes must either be assumed or parameterized using simple cloud models.

Cloud-resolving models (CRMs) are another type of tool that can be used to study convectively coupled tropical waves. With current computational resources, we can conduct explicit simulations of radiative–convective equilibrium (RCE) in planetary-sized domains, allowing interactions between convection and dynamics on a wide range of time and space scales. Mostly these simulations have been in two dimensions (2D; e.g., Oouchi 1999; Grabowski and Moncrieff 2001; Peng et al. 2001; Oouchi and Yamasaki 2002; Grabowski 2003), although 3D simulations using state-of-the-art supercomputers (Tomita et al. 2005), as well as smaller computers through clever means (Kuang et al. 2005), are rapidly joining the fray.

As an example from the realm of 2D studies, Grabowski and Moncrieff (2001) performed a 30-day simulation of RCE in a nonrotating, periodic domain with a spatially uniform sea surface temperature (SST), a spatially uniform radiative cooling profile, and an imposed barotropic mean flow of $-10\ \mathrm{m\,s^{-1}}$. They obtained spontaneous development of a series of large-scale gravity wave disturbances whose dispersion characteristics and longitude–height structures were found to strongly resemble observations of a particular type of convectively coupled equatorial wave—the Kelvin wave (Nakazawa 1988; Takayabu and Murakami 1991; Wheeler et al. 2000; Straub and Kiladis 2003). Such agreement is encouraging and suggests that 2D CRMs, although somewhat artificial, can still be used to gain insights into real-world phenomena. The challenge is to cast the model output in terms that can facilitate understanding.

This paper describes an analysis of a similar 2D CRM simulation in which large-scale convectively coupled gravity waves spontaneously develop. As part of the analysis, we use a vertical-mode transform algorithm to project profiles of winds, temperature, and heating rate onto the vertical modes of the model's base-state atmosphere (as in Kasahara and Puri 1981; Mapes and Houze 1995; Haertel and Johnson 1998; Grabowski et al. 2000). A cloud-partitioning algorithm is also used to sort sufficiently cloudy grid columns into three categories: shallow convective, deep convective, and stratiform anvil (as in Tao and Simpson 1989; Xu 1995; Lang et al. 2003). Through this approach, we seek to characterize the structures and energetics of the large-scale waves in a low-order truncated space suitable for qualitative reasoning and conceptual understanding, as well as for the design and diagnosis of parameterizations for large-scale models.

The organization of this paper is as follows. The next two sections briefly describe the CRM, the experiment setup, and the cloud-partitioning method. Some general features of the simulation are discussed in section 4. Section 5 outlines the theory of the vertical-mode transform and discusses its implementation. Results from the vertical-mode analysis are presented in section 6. Our main findings are summarized and discussed in section 7.

2. Numerical model and experiment setup

The simulation is performed using the 2D version of the System for Atmospheric Modeling (SAM), developed by M. Khairoutdinov at Colorado State University (CSU). A brief description of the CSU SAM is given below. A more detailed description can be found in Khairoutdinov and Randall (2003).

The model is based on an anelastic system of equations consisting of five prognostic variables: the horizontal and vertical components of the velocity vector ($\mathbf{u} = u\mathbf{i} + w\mathbf{k}$), the mixing ratio of water vapor plus nonprecipitating water substance (r_{np}), the mixing ratio of precipitating water substance (r_p), and the liquid/ice water static energy (h_l). The model equations are solved using finite-difference approximations on an Arakawa C-grid with periodic lateral boundary conditions

and free-slip, rigid-lid conditions imposed at the upper and lower boundaries. Subgrid-scale turbulent fluxes are parameterized using a simple Smagorinsky-type closure, with the turbulent mixing coefficient proportional to the square of the local vertical grid spacing. The model includes a bulk microphysics parameterization with five types of hydrometeors: cloud water, cloud ice, rain, snow, and graupel.

The setup of the experiment is as follows. The computational domain extends 8192 km in the horizontal and 28 km in the vertical. The horizontal grid spacing is spatially uniform at 2 km, while the vertical grid spacing stretches from 50 m near the surface to 500 m at and above 5 km. The radiative cooling is 1.5 K day^{-1} between the surface and 250 mb (~10 km), decaying linearly to zero at 200 mb (~12 km). The SST is spatially uniform and fixed at 300 K. To minimize possible interactions between convection and a domain-averaged horizontal flow, a spatially uniform relaxation term $-\overline{u}/\tau$ is added to the horizontal momentum equation, where $\overline{u}$ is the domain-averaged horizontal wind and $\tau = 4$ h is the relaxation time scale. Rayleigh damping of perturbation winds, temperature, etc. is also applied in the uppermost 8 km to remove energy from gravity waves reflected off of the upper boundary. The effects of planetary rotation are not considered.

The simulation begins with random small-amplitude temperature and moisture perturbations added to an otherwise resting and stably stratified atmosphere. The initial sounding is representative of equilibrium conditions from a previous 45-day run, identical to the one described above but with a smaller 1024-km computational domain. The simulation lasts for 15 days, with model output saved at 10-min intervals.

3. Cloud partitioning method

This section describes the method used to separate sufficiently cloudy grid columns into three categories: shallow convective, deep convective, and stratiform anvil. Following Xu (1995), the method is based on observations of both the structures and kinematics of tropical mesoscale convective systems (e.g., Houze 1977; Zipser 1977; Zipser et al. 1981). Briefly, deep convective regions are characterized by relatively intense vertical motion and appear as vertically developed cumuliform clouds with bases typically located beneath the melting layer. Stratiform regions, on the other hand, are characterized by relatively weak vertical motion and appear as elevated cloud layers with bases typically located above the melting layer. A similarity between deep convective and stratiform regions is that both have cloud tops in the upper troposphere. Shallow convective regions, on the other hand, are typified by cloud tops in the lower to middle troposphere. The one exception is when shallow convective clouds develop beneath upper-level anvil clouds such that there are multiple cloud tops. In this situation, the column is perhaps best viewed as being part of the shallow convective region, if the low-level convection is especially vigorous (or the upper-level cloudiness is especially diffuse), but as being part of the stratiform region otherwise.

The above observations and considerations are encoded in the method as follows. First, we define the cloud-top height $Z_{\rm CT}$ as the height of the uppermost grid cell with a total condensed water/ice mixing ratio $r_c = r_p + r_{\rm np}$ greater than either (i) 0.1 g kg^{-1}, if the column maximum of r_c exceeds this value, or (ii) 0.01 g kg^{-1}, otherwise. The cloud-base height $Z_{\rm CB}$ is defined as the height of the lowermost grid cell with $r_{\rm np} < 0.01$ g kg^{-1}. Additional parameters considered in the method are the maximum absolute value of the in-cloud vertical velocity $|w_{\rm max}|$ and the cloud condensate paths in the lower (0–4 km; CCP$_L$), middle (4–8 km; CCP$_M$), and upper (8–12 km; CCP$_U$) troposphere, where each path is divided by the total water vapor path of the time-mean sounding so that CCP has units of grams per kilogram.

Deep convective regions are identified first in the method. They are defined as all "deep cores" plus the two adjacent columns. Deep cores must satisfy *each* of the following three requirements: 1) $Z_{\rm CT} > 7$ km, 2) CCP$_M > 25$ g kg^{-1}, and 3) $|w_{\rm max}| > 3$ m s^{-1}, with $Z_{\rm CB} < 4$ km; or else the single requirement $|w_{\rm max}| > 9$ m s^{-1} (to capture vigorous tilted or elevated cells above an unsaturated lower troposphere). Shallow convective areas are identified next in the method, again via cores and neighbors (provided these columns are not already assigned as deep). Shallow cores must satisfy *any one* of the following three requirements: 1) $Z_{\rm CT} < 7$ km, with $Z_{\rm CB} < 2.5$ km; 2) CCP$_L > 30$ g kg^{-1}, with CCP$_U < 15$ g kg^{-1}; or 3) $|w_{\rm max}|$ in the lowest 3 km exceeds 3 m s^{-1}. After the shallow and deep convective regions have both been identified, the remaining columns with a total condensed water/ice path exceeding 10 g m^{-2} are masked as stratiform.

This approach is similar to that of Xu (1995) but differs from that of most other studies, which use the spatial distribution of the surface precipitation as the primary separation criterion (e.g., Tao and Simpson 1989; Tao et al. 1993; Caniaux et al. 1994; Lang et al. 2003). Because our method is basically an extension of Xu's (1995) Wmax method, adding cloud-height (Z_C) considerations, we refer to it for convenience as the Zc-Wmax method.

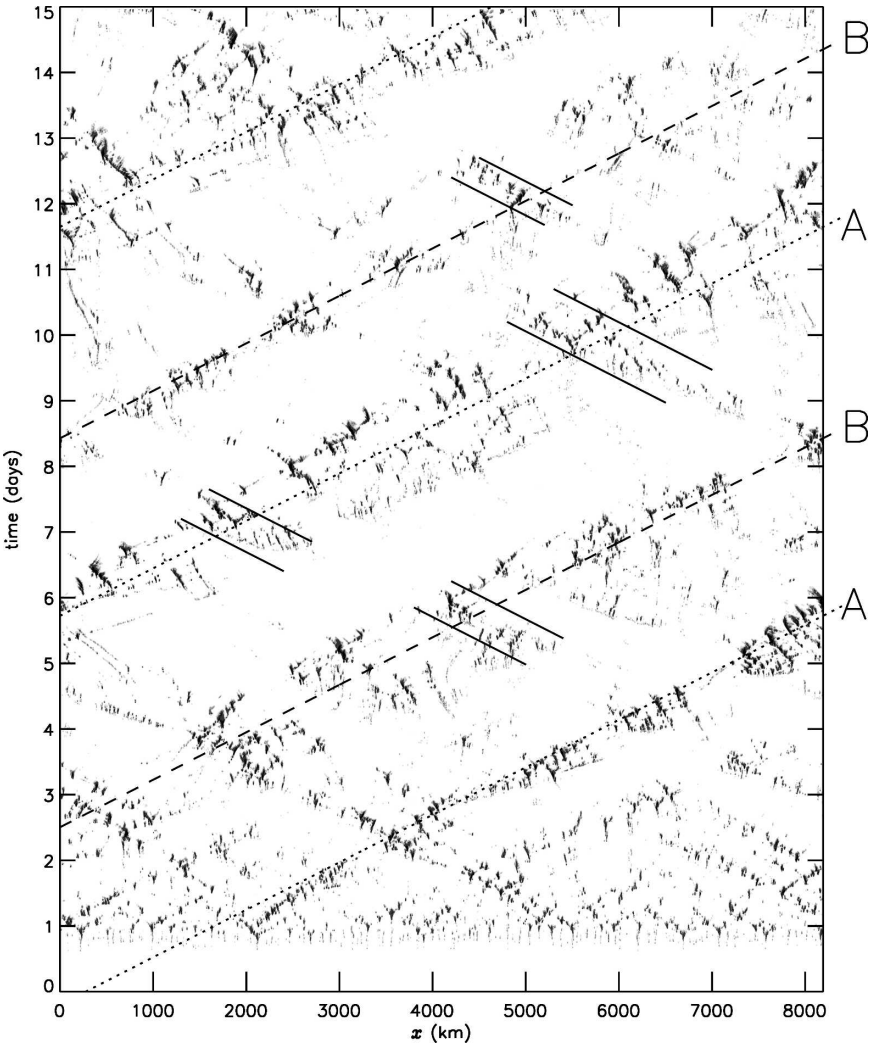

FIG. 1. Time–longitude diagram of the simulated surface precipitation rate P. Light and dark shading denote values greater than 2 and 20 mm h^{-1}, respectively. Dotted and dashed lines (labeled A and B, respectively) identify the convective envelopes of two large-scale convectively coupled gravity waves moving rightward at speeds of 16 m s^{-1}. Pairs of sloping lines highlight several occasions where individual cloud clusters within A and B appear to be organized into intermediate-scale disturbances moving leftward.

4. General features of the simulation

a. Organization of convection

Figure 1 illustrates the general patterns of convective organization in the simulation. Shading indicates the space–time evolution of the surface precipitation rate P, a proxy for convective activity. Starting from a more-or-less random distribution of cells on day 1, convection spontaneously becomes organized into two distinct large-scale envelopes (indicated by the dotted and dashed lines labeled A and B) that move rightward at speeds of about 16 m s^{-1}. The envelopes are typically composed of many small-scale contiguous precipitation features, later referred to as "cloud clusters," with lifetimes in the range 2–12 h and spatial scales in the range 20–100 km. Many of the cloud clusters propagate leftward at speeds in the range 3–9 m s^{-1}. Some, however, remain stationary or propagate slowly rightward. There are also a number of occasions where individual cloud clusters within A and B appear to be organized into intermediate-scale disturbances moving leftward at speeds in the range 16–18 m s^{-1} (highlighted by pairs of sloping lines in Fig. 1). This hierarchical pattern of convective organization, including the propagation speeds of the large-scale envelopes, is broadly similar to that observed in association with convectively coupled Kelvin waves (Nakazawa 1988; Straub and Kiladis 2002), as well as that found in previous 2D CRM studies

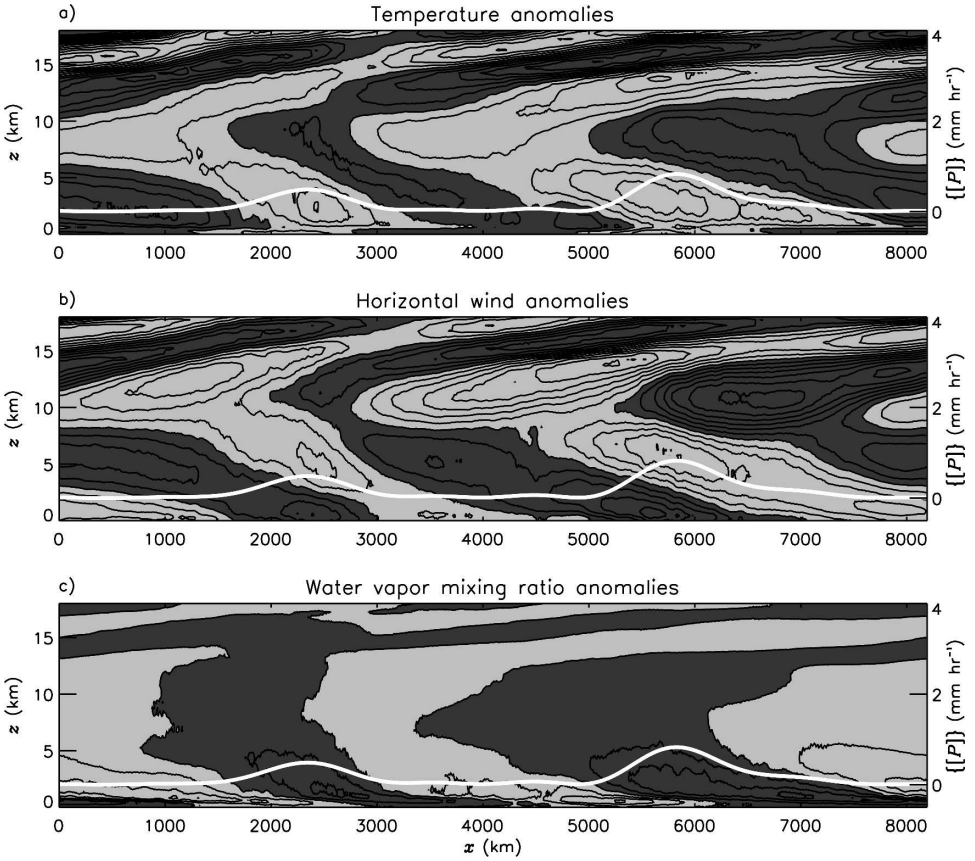

FIG. 2. Longitude–height distributions of (a) temperature $[T]$, (b) horizontal wind $[u]$, and (c) water vapor mixing ratio $[r]$ anomalies, where brackets denote the time average between days 5 and 11 in a reference frame moving eastward at 16 m s^{-1}. Contour intervals are 0.4 K, 1.3 m s^{-1}, and 0.5 g kg^{-1} with dark and light shading denoting positive and negative values, respectively. The heavy white curves in each panel depict the composite distribution of the surface precipitation rate $\{[P]\}$ (with axis given to the right), where the braces denote application of a low-pass Lanczos filter with a cutoff wavelength of 1024 km.

(Grabowski and Moncrieff 2001; Peng et al. 2001; Grabowski 2003). On the basis of this similarity, we refer to the large-scale convective envelopes and their associated circulations as large-scale convectively coupled gravity waves.

A curious feature of the large-scale waves is that they have a preferred direction of propagation (rightward), even though the model governing equations are symmetric with respect to horizontal direction. During the course of this work, we performed four additional simulations, each identical except for having slightly different initial conditions. Results in all cases were found to be similar to those discussed above, but with leftward-moving waves appearing prominently in two of the simulations and both leftward- and rightward-moving waves appearing prominently in the two others (not shown). Thus it appears that the direction of large-scale wave propagation is determined simply by chance.

b. Composite wave dynamical structures

Composite dynamical structures of the large-scale waves were obtained by averaging the model output between days 5 and 11 in a reference frame moving rightward at 16 m s^{-1}. Figures 2a–c show the resulting anomaly patterns of temperature $[T]$, horizontal wind $[u]$, and water vapor mixing ratio $[r]$, where brackets denote the comoving time average. The thick gray curves toward the bottom of each panel depict the zonal distribution of the surface precipitation $[P]$, smoothed for clarity using a low-pass Lanczos filter with a cutoff wavelength of 1024 km. As with observations of convectively coupled Kelvin waves (e.g., Takayabu and Murakami 1991; Wheeler et al. 2000; Straub and Kiladis 2003), the dynamical signals associated with the waves display a boomerang-like structure with the elbow of the boomerang located in the upper

troposphere. The angle of the tilt implies upward propagation of wave energy in the stratosphere and downward propagation below, indicating that the source of wave energy is located in the upper troposphere (near ~10 km). The rainy portion of the waves is anomalously cool in the lower troposphere (with a thin surface cold pool lagging somewhat), anomalously warm in the upper troposphere, and anomalously cool at the level of the tropopause (~13 km). Near the surface, convergence of the horizontal winds leads precipitation by roughly a quarter wavelength, while at upper levels (~10 km) precipitation and divergence are roughly in phase with one another. Water vapor mixing ratio anomalies show relatively large-amplitude fluctuations at low levels and weaker fluctuations aloft. The low-level anomalies tilt westward with height in a fashion similar to that of the temperature field but with opposite sign. Precipitation is strongest when air is anomalously dry in the boundary layer and wet aloft.

c. Structures and evolution of small-scale cloud clusters

To give a sense of the simulation's inner details, Figs. 3a–g depict the structures and evolution of a leftward-propagating cloud cluster (labeled cc3 in Fig. 4) that developed roughly 8.5 days into the simulation at $x \cong 3150$ km. The evolution can be divided into three stages: growth, mature, and decay. During its growth stage (Figs. 3a and 3b), the cluster appears as a roughly 60-km-wide patch of shallow convective cells whose characteristic depth and intensity increase with time. As the cells deepen, some of their rain evaporates before reaching the surface, resulting in the formation of a spreading surface-based cold pool (thick contour), first apparent 20 min prior to Fig. 3c (not shown). Meanwhile, an earlier decaying cloud system, with its own distinct cold pool (thick contours at left in Figs. 3a and 3b), moves rightward toward the developing patch of cells, but dies out just before reaching them.

The cluster during its mature stage (Figs. 3c–e) appears as a left-moving squall system consisting of a leading band of vigorous convective cells (evolving from shallow to deep) and a trailing stratiform anvil cloud. The convective cells are initiated at the left edge of the system's cold pool and penetrate upward to ~13–14 km. Convective cells are also initiated at the right edge of the cold pool, but remain confined to the lower troposphere.

During its decay stage (Figs. 3f–h), the cluster appears as a horizontally extensive anvil that becomes increasingly ragged and thin with time. The cold pool continues to spread in both directions; however, no new deep convective cells are initiated. A possible explanation for this can be found in Fig. 4, which shows that the demise of cc3 (as well as ccl and cc2) occurred when it encountered a wedge of warm temperature anomalies associated with the large-scale wave disturbances. This warmth reduces cloud buoyancy, by definition, and is also correlated with dryness (cf. Fig. 2), which gets entrained into growing cumuli. Together, these effects apparently inhibit convective development and terminate the positive feedback associated with cold pool/gust front triggering.

d. Partitioning of the convective apparent heat source

Returning to the subject of the large-scale wave disturbances, we wish to understand how these propagating circulation and temperature anomaly patterns are excited and maintained against the effects of dissipation. The main mechanism is presumably diabatic heating, which we can categorize on the basis of cloud type. Figure 5a shows composite profiles of the "convective apparent heat source" $Q1$ [defined similarly to Yanai et al. (1973); see the appendix for details] in shallow convective, deep convective, and stratiform anvil regions. For ease of comparison, the profiles are expressed as heating over the entire domain area.

The deep convective profile exhibits heating through the depth of the free troposphere with a peak at 6 km. There is also a shallow layer of weak cooling in the lowest 1 km associated with evaporation of precipitation in convective downdrafts. The stratiform profile consists of weaker heating in the upper half of the troposphere, with a peak at 9 km, and cooling below, with a peak at 3 km. The shapes of these profiles are by now familiar: for example, they are similar to those discussed by Houze (1982, 1989, 1997), diagnosed by Johnson and Young (1983), or obtained by Xu (1995) using his Wmax method applied to explicitly simulated squall-line systems (see also Tao and Simpson 1989; Caniaux et al. 1994; Lang et al. 2003).

The shallow convective heating profile exhibits relatively intense cooling in the boundary layer, overlain by heating from 0.5- to 5-km altitude with a peak at ~1 km. The vertically integrated heating and PBL cooling shows that our shallow convective category is dominated by precipitating congestus clouds (e.g., Fig. 3b), not merely nonprecipitating trade cumuli. The distinct layer of weak warming in the upper troposphere reflects the occasional presence of weakly active stratiform anvils above vigorous shallow convective cells (see, e.g., Figs. 3d and 3e).

Deep convective columns can further be separated into two subcategories: "high based" ($Z_{CB} \geq 2.5$ km) and "low based" ($Z_{CB} < 2.5$ km), whose composite

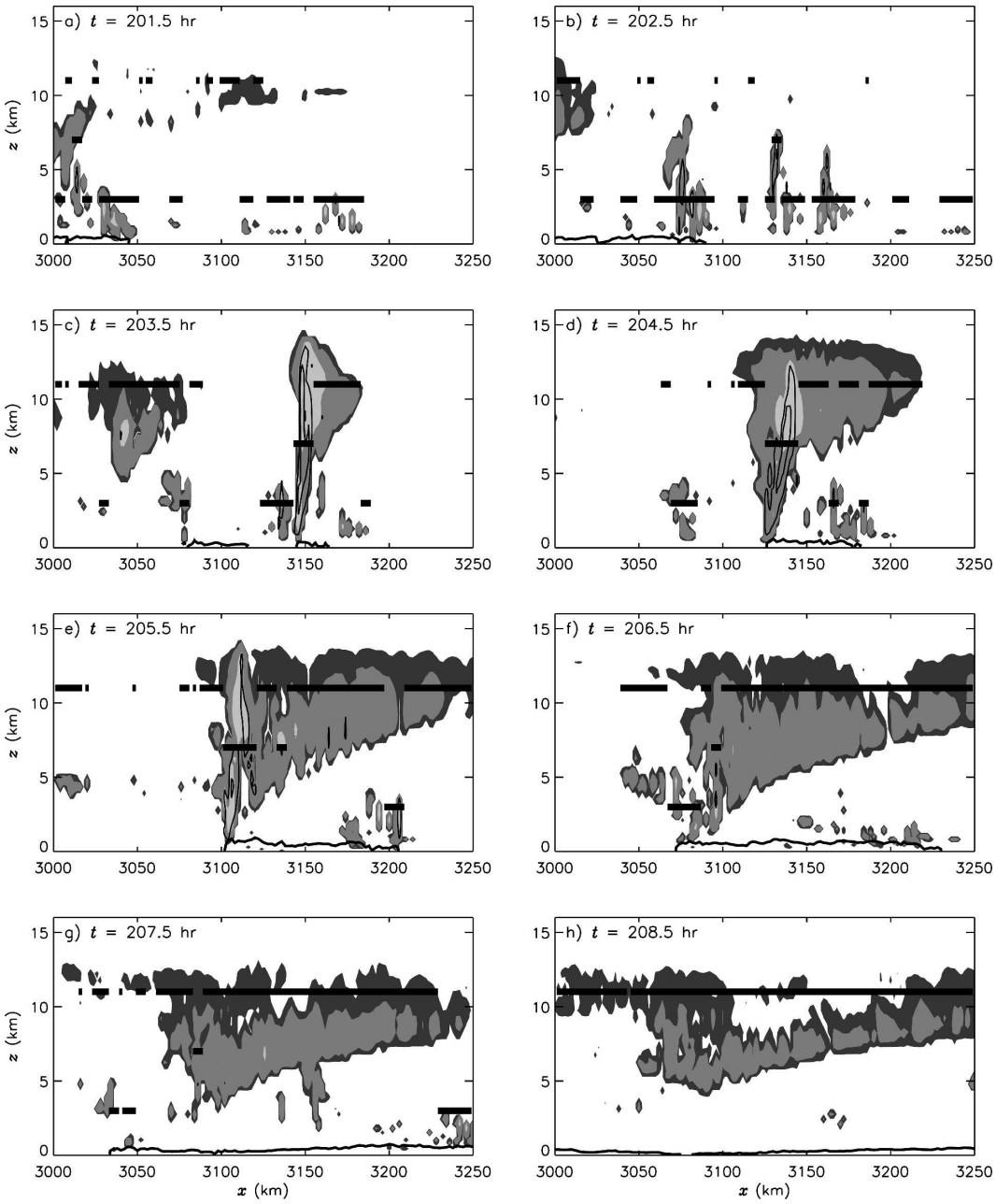

FIG. 3. Hourly snapshots of the left-moving cloud cluster labeled cc3 in Fig. 4. Shading denotes cloud water mixing ratios of 0.01. 0.1, and 1.0 g kg^{-1}, while thin contours denote vertical velocities of 3 and 9 m s^{-1}. Heavy contours denote a dry static energy of 296 K (used here to identify the boundaries of convectively generated surface-based cold pools). Thick horizontal lines at 3-, 7-, and 11-km altitudes denote columns masked by the Zc-Wmax algorithm as shallow convective, deep convective, and stratiform anvil, respectively.

heating profiles are shown in Fig. 5b. The low-based profile (light line) has heating through the depth of the free troposphere with a peak at around 3 km. The high-based profile, which captures columns with low-level convective downdrafts, shows heating in the middle to upper troposphere and cooling below. Because the shape of the high-based profile is broadly similar to the stratiform profile, one could argue that the arbitrary parameters of the convective–stratiform partitioning algorithm should be adjusted to eliminate this redundancy. Table 1, however, shows that the averaged kinematic properties of high-based columns are almost identical to those of low-based columns, while differing markedly from stratiform columns: the peak updraft

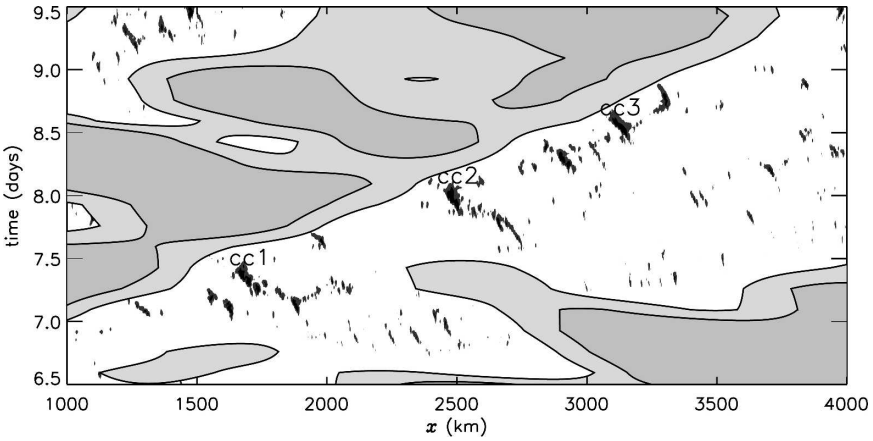

FIG. 4. Similar to Fig. 1 but for a 3000-km subdomain centered at $x = 2500$ km during a 3-day period starting on day 6.5. Symbols denote three distinct leftward-moving cloud clusters, while contours with shading denote regions where the vertically averaged temperature anomaly in the layer $z \cong 800$–1500 km (smoothed in time and space for clarity) is positive (light shading) or exceeds 1 K (darker shading).

speeds are roughly a factor of 10 larger, while the fractional area coverages are about 200 times smaller. On the basis of these differences, we regard the low- and high-based profiles as being representative of deep convective cells during their early and later stages of development, respectively, while still acknowledging that an ambiguous middle ground exists, for example, the "intermediate" profiles of Mapes and Houze (1992), or the "transition zone" in squall lines identified by the Houze and Johnson research groups. The reason to distinguish between these two subtypes of deep convection will become clearer in section 6, where it is shown that their roles in the generation and maintenance of the large-scale waves are distinctly different.

Distributions of shallow convective, deep convective, and stratiform heating processes in the large-scale wave composite space of Fig. 2 are shown in Fig. 6. Shallow convective heating peaks roughly 100 km to the right of the most intense deep convective heating, implying a ~2 h lead, given a large-scale wave propagation speed of 16 m s^{-1}. Stratiform heating peaks about 150 km to the left, implying a ~3 h delay. At larger scales, the leading edge of the shallow convective heating is positioned roughly 1000 km out ahead of the leading edge of the deep convective heating, implying a gradual (~20 h) deepening of shallow convection prior to the onset of deep convection. This is much farther than stratiform heating extends in the back, yielding an important asymmetry in the total heating (Fig. 6d).

Based on the cloud snapshots in Fig. 3, we interpret the relatively short delays in cloud heating to be a reflection of the cloud cluster life cycle described earlier. The more gradual buildup of shallow convection, on the other hand—seen also in observations by Takayabu et al. (1996), Haertel and Johnson (1998), Straub and Kiladis (2003), and Mapes et al. (2006)—seems to involve a more scale-separated interaction between short-lived convective clouds and broader, systematic wave-driven environmental changes. This is supported by Fig. 7d, which shows that the wedge of the shallow convective heating on the right side of the convective envelopes is almost perfectly coincident with the wedge of cold temperature anomalies, suggesting that the depth and intensity of convection is strongly modulated by the density field in the lower free troposphere. Moisture anomalies, however, are also coincident with this wedge (cf. Figs. 2a and 2c), and surely play some role in modulating clouds, as well as being strongly influenced by them. Separating the influences of temperature and moisture on convection is therefore not simple and remains an important challenge for future research.

5. The vertical-mode transform: Theory and implementation

The primary objective of this study is to quantify the relative roles of shallow and deep cloud types and dynamic vertical wavelengths in the development and maintenance of the large-scale wave disturbances. To achieve this objective, we used the vertical-mode transform algorithm of Fulton and Schubert (1985; hereafter FS85) to perform a vertical-mode decomposition of the model output. This section reviews FS85's theory of the transform and discusses its implementation, with results given in section 6.

a. Theory

FS85 show that the hydrostatic primitive equations (linearized about a state of rest, with reflecting-type

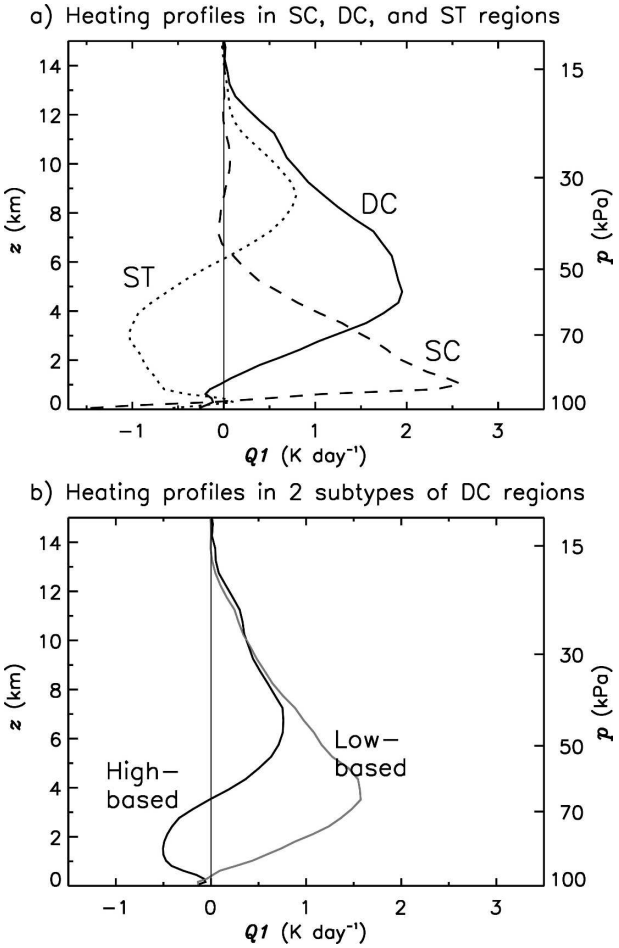

FIG. 5. (a) Composite profiles of the convective apparent heat source $Q1$ in shallow convective (SC, dashed), deep convective (DC, solid), and stratiform anvil (ST, dotted) regions. (b) Similar to (a) but for heating in "high based" ($Z_{CB} \geq 2.5$ km, dark curve) and "low based" ($Z_{CB} < 2.5$, light curve) deep convective regions. For ease of comparison, the profiles are expressed as heating rate over the entire domain area.

upper and lower boundary conditions) may be transformed into a set of n linearly independent shallow-water equations describing the horizontal evolution of n vertical modes. In the absence of planetary rotation and assuming 2D geometry, these equations take the form

$$\frac{\partial u_n}{\partial t} + \frac{\partial \phi_n}{\partial x} = 0 \tag{1}$$

and

$$\frac{\partial \phi_n}{\partial t} + c_n^2 \frac{\partial u_n}{\partial x} = \dot{\Phi}_n, \tag{2}$$

where u_n and ϕ_n are the modal amplitude coefficients of the horizontal wind u and geopotential ϕ anomalies respectively, c_n corresponds to the modal gravity wave speed, $\dot{\Phi}_n$ is the geopotential source due to heating for each mode, and the effects of horizontal momentum forcing have been neglected for simplicity.

TABLE 1. Composite kinematic properties of shallow convective, deep convective (separated into high- and low-based components), and stratiform regions, where A_{frac} is the fractional area coverage, P_{vol} is the fraction of the total surface precipitation volume, and w_{up_max} and $w_{down-max}$ are the column-maximum updraft and downdraft speeds, respectively.

Region	A_{frac} (%)	P_{vol} (%)	w_{up_max} (m s^{-1})	$w_{down-max}$ (m s^{-1})
Shallow convective	12.5	33.6	0.6	0.5
Deep convective (high based)	0.2	23.7	5.5	2.4
Deep convective (low based)	0.2	19.3	5.0	2.5
Stratiform	13.7	23.4	0.6	0.6

FS85 use a vertical-mode transform to arrive at (1) and (2). The transform is given in pressure coordinates by

$$u_n(x, t) \equiv \frac{1}{p_B - p_T} \int_{p_T}^{p_B} u(x, p, t)\Psi_n(p)\, dp, \tag{3}$$

where the transform kernel Ψ_n is the vertical structure function applicable to the horizontal wind u (and geopotential ϕ) anomalies and p_T and p_B denote the pressures at the top and bottom boundaries, respectively. The vertical structure functions Ψ_n (and their associated "phase speeds" c_n) are obtained as eigensolutions of the vertical structure problem, given by

$$\left.\begin{aligned} -\frac{d}{dp}\left(p^2\overline{N}^2\frac{d\Psi_n}{dp}\right) &= c_n^{-2}\Psi_n \\ B_T\{\Psi_n\} = B_B\{\Psi_n\} &= 0 \end{aligned}\right\}, \tag{4}$$

where $\overline{N}$ is the Brunt–Väisälä frequency of the basic state and $B_T\{\,\}$ and $B_B\{\,\}$ are functionals expressing conditions at the top and bottom boundaries, respectively (see FS85 for details).

An important property of solutions to (4) is that the eigenfunctions Ψ_n form a complete, orthogonal set. This means we can expand any function as

$$u(x, p, t) = \sum_{n=0}^{\infty} u_n(x, t)\Psi_n(p), \tag{5}$$

where the error in the summation converges uniformly to zero as n goes to infinity. From this expression, along with (1) and (2), we see that solutions to the linear hydrostatic primitive equations may be obtained by solving the shallow-water equations for each vertical

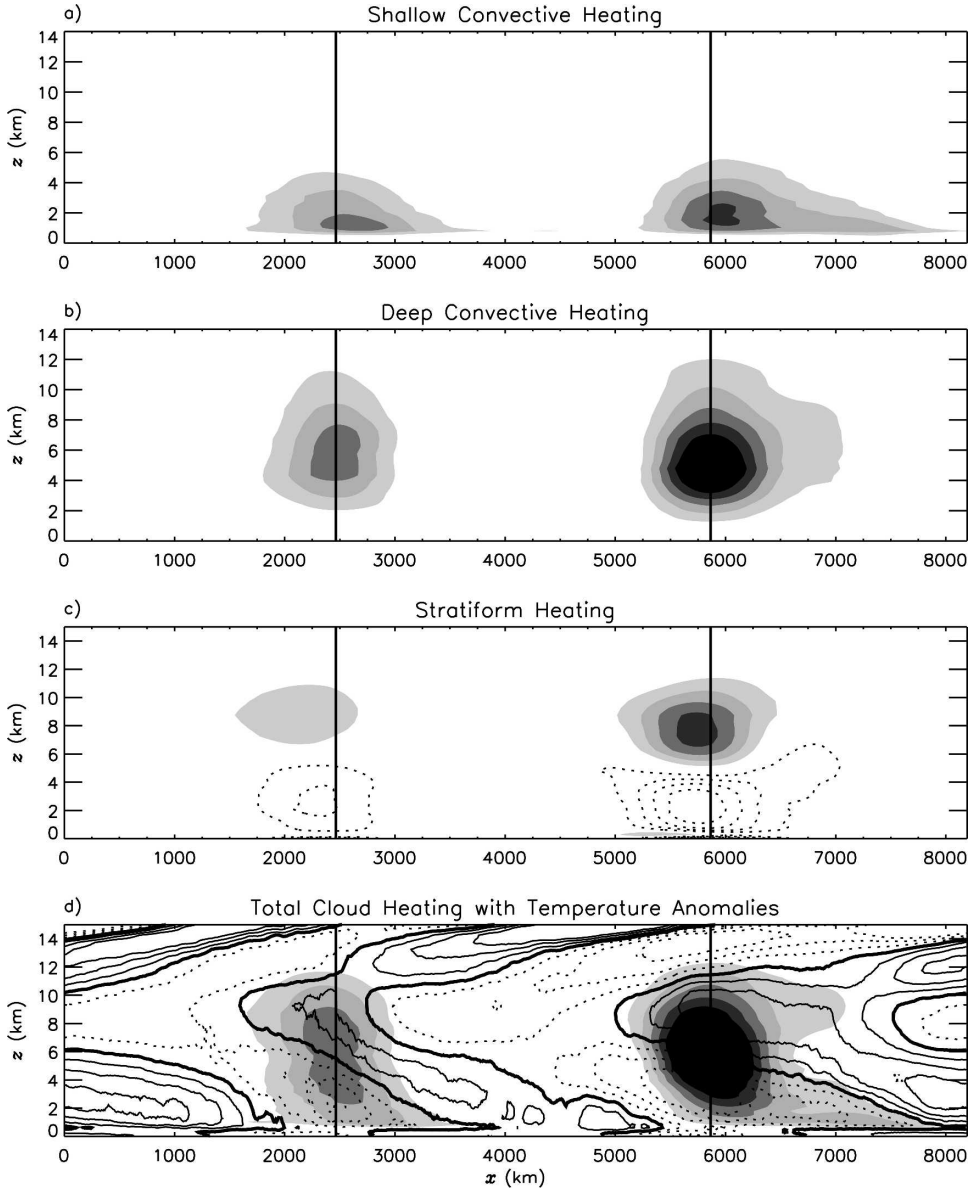

FIG. 6. Similar to Fig. 2 but for the apparent heating distributions [$Q1$] in (a) shallow convective, (b) deep convective, and (c) stratiform regions, along with (d) the total cloud heating (given by the sum of the top three panels) and temperature anomalies. In (a), (b), and (d) only positive heating rates are shown, with shading intervals of 2 K day^{-1} in (a) and (b) or 1 K day^{-1} in (d). In (c), both positive (shaded) and negative (contoured) heating rates are shown with intervals of 1 K day^{-1}. Temperature anomalies are contoured in (d), with positive and negative values given by the solid and dotted contours, respectively, and the zero line given by the heavy solid contour. Thick vertical lines in each panel denote the x location of the local maxima of column-integrated deep convective heating.

mode and then summing the results. Equation (5) also shows that, owing to the presence of an upper boundary, the spectrum of modes is discrete, in contrast with the real atmosphere which does not have an upper boundary, and thus supports a continuum of modes. Mapes (1998), however, showed that changing the height of the upper boundary produces merely different discretizations of consistent underlying vertical spectral "bands." Thus, despite the formal correctness of objections to vertical-mode approaches, such approaches can be considered useful, especially if the height of the upper boundary is chosen with care and/or the modes are appropriately grouped and reinterpreted as spectral bands.

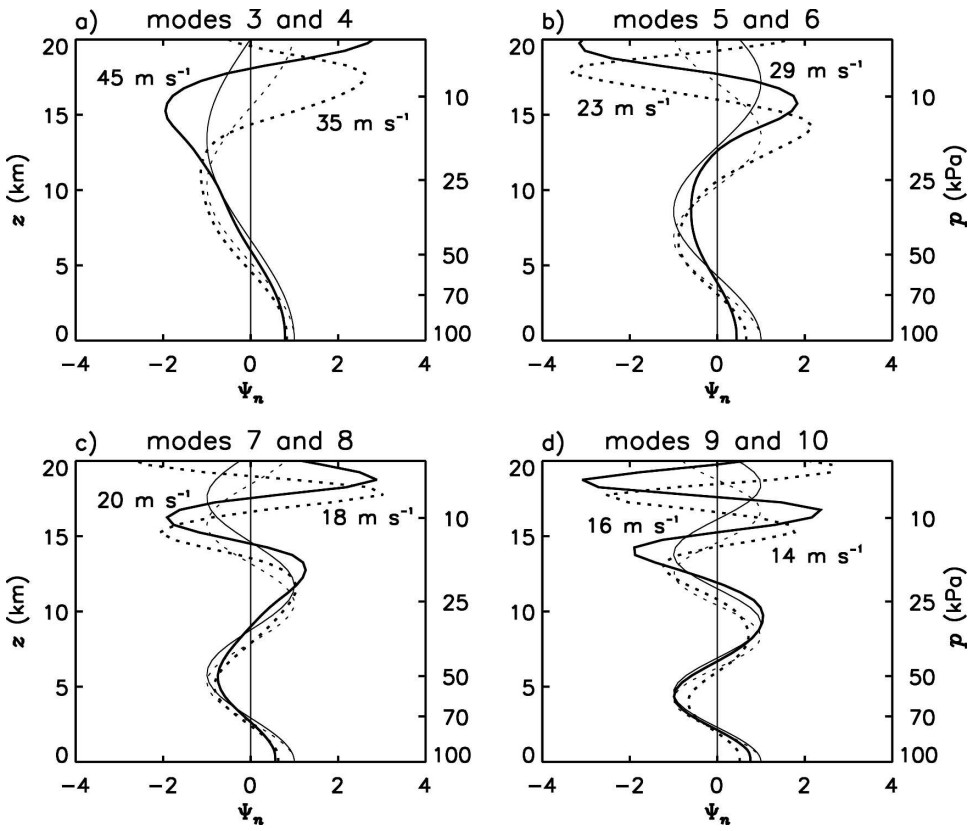

FIG. 7. Vertical structure functions Ψ_n valid for the horizontal wind u and geopotential ϕ anomalies in the lowest 20 km for modes n = 3–10. Thick solid (dotted) curves depict the structure function associated with the even (odd) mode index n, while labels denote the corresponding phase speed c_n. The thin curves are idealizations for comparison, given by pure cosine functions with vertical wavelengths L_{zn} in Table 2.

b. Implementation

Solutions to the vertical structure problem were obtained using the numerical algorithm of FS85 with the basic-state virtual temperature profile in the simulation used as input and with a spectral truncation of 65 modes. To ensure consistency of the solutions with the vertical boundary conditions of the CRM, the pressures levels p_T and p_B were specified as the top and bottom pressure levels in the CRM (~14 and 1000 mb, respectively).

After obtaining the discrete spectrum of modes, we next used a discrete version of the vertical transform (3) to calculate spectra of u_n, ϕ_n, and $\dot{\Phi}_n$ at each grid column and at each time. For example, the spectrum of the horizontal winds was obtained as

$$u_n(x, t) = \frac{1}{\Delta p_{\text{tot}}} \sum_k \tilde{u}(x, p_k, t)\psi_n(p_k)\Delta p_k, \qquad (6)$$

where the tilde denotes interpolation of the simulated profile from the z-coordinate system of the CRM to the p-coordinate system of the ψ_n (given by the set of p_k pressure levels with vertical spacing Δp_k) and Δp_{tot} represents the sum of Δp_k over all k.

1) GENERAL PROPERTIES OF THE CALCULATED SPECTRUM

Table 2 lists the propagation speeds c_n, equivalent depths $h_n = c_n^2/g$, and "bulk" vertical wavelengths in the troposphere L_{zn} of modes n = 0–14. Here, a value of L_{zn} is assigned based on the analytic expression for waves in a Bousinnesq atmosphere with uniform stratification; that is,

$$L_{zn} \equiv \frac{2\pi c_n}{N^*}, \qquad (7)$$

where $N^* = 1.02 \times 10^{-2}$ s^{-1} is the averaged value of the Brunt–Väisälä frequency in the lowest 14 km. For example, n = 7 has a propagation speed of 23 m s^{-1} and, thus, a vertical wavelength L_{zn} comparable to the depth of the troposphere, while n = 3 has a speed of

TABLE 2. Phase speed c_n, equivalent depth h_n, and "bulk" vertical wavelength in the troposphere L_{zn} (see text for details) of modes $n = 0$–14. For convenience, values of c_n and h_n have been rounded to the nearest integer.

n	c_n (m s^{-1})	h_n (m)	L_{zn} (km)
0	302	9384	180.9
1	123	1542	73.3
2	63	409	37.7
3	45	206	28.2
4	35	123	20.7
5	29	85	18.1
6	23	54	13.7
7	20	39	11.7
8	18	32	10.6
9	16	24	9.2
10	14	20	8.4
11	13	17	7.6
12	12	14	6.9
13	11	12	6.3
14	10	10	5.9

45 m s^{-1} and, thus, a wavelength correspondingly twice as large. Although the parameter L_{zn} is only approximate, Fig. 8 shows that the calculated structure functions are reasonably well summarized by these L_{zn} vertical wavelengths. More strictly, the structure functions have a vertically varying local curvature that depends on the shape of the background static stability profile.

2) TEMPERATURE STRUCTURE FUNCTIONS

In addition to the vertical structure functions Ψ_n valid for u and ϕ, the hydrostatic relation,

$$\frac{\partial \phi}{\partial \ln p} = -RT, \tag{8}$$

where R is the dry air gas constant, implies a corresponding set of (virtual) temperature structure functions, given in pressure coordinates by

$$\Im_n(p) = T_n \frac{c_n}{c_R}\left(\frac{d\Psi_n}{d\ln p}\right) = T_n \xi_n(p). \tag{9}$$

Here ξ_n is the nondimensional part of $\Im_n$ (analogous to Ψ_n), c_R is a constant phase speed of convenience whose magnitude is equal in number to the dry air gas constant R (i.e., $c_R = 287$ m s^{-1}), and T_n is a normalizing amplitude coefficient, defined as

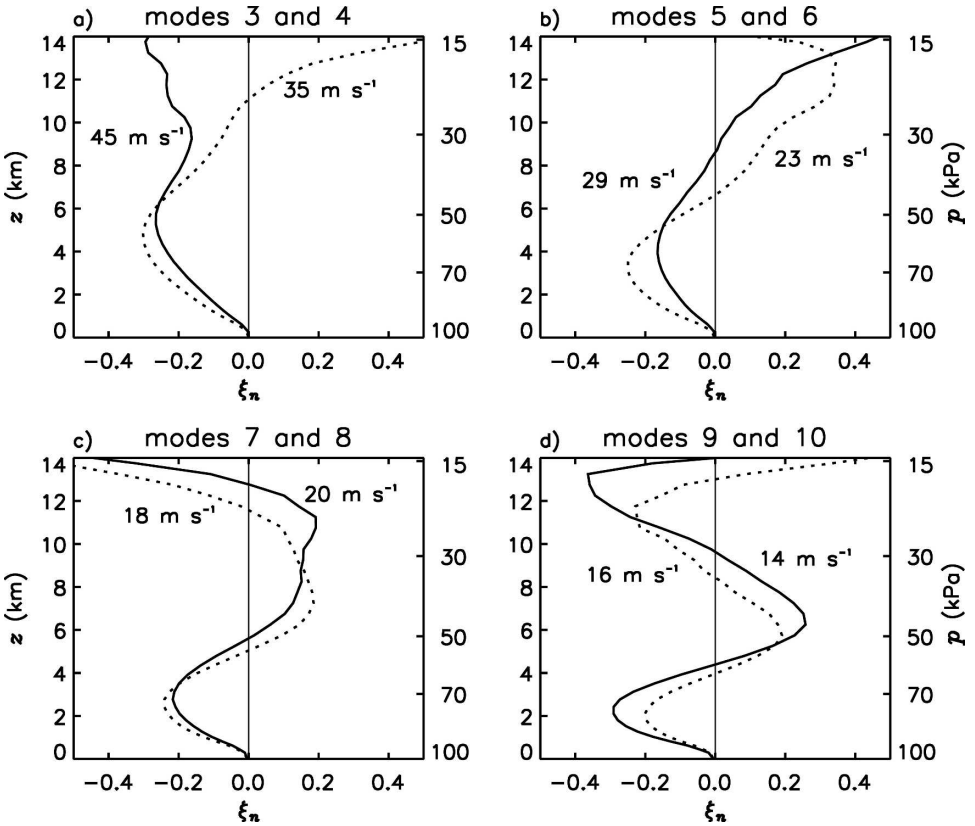

FIG. 8. Similar to Fig. 7 but for the nondimensional temperature structure functions ξ_n in the lowest 14 km.

$$T_n \equiv -\left(\frac{c_R}{R}\right)\frac{\phi_n}{c_n} = -\alpha_R\frac{\phi_n}{c_n} = -\left(\frac{1\text{ K}}{1\text{ m s}^{-1}}\right)\frac{\phi_n}{c_n}, \tag{10}$$

with α_R being a units conversion factor (with amplitude unity) that gives T_n the units of temperature. The amplitude coefficient T_n is introduced because it makes the characteristic amplitude of ξ_n remain more or less independent of n, thereby facilitating structure function comparisons in Figs. 7 and 8. The "spectrum" of T_n characterizing a given temperature profile is thus a measure of both the sign and amplitude of the modal temperature anomalies, just as the "spectra" of u_n and ϕ_n depict the sign and amplitude of the modal contributions to their respective fields. Here, the sign convention is that T_n and u_n take the same sign as the nth mode's contribution to temperature and horizontal wind anomalies near the surface.

Just as T_n is a measure of the sign and amplitude spectrum of modal temperature anomalies, the spectrum of heating can be defined as

$$Q_n \equiv -\alpha_R\frac{\dot{\Phi}_n}{c_n}. \tag{11}$$

The transformed system (7) and (8) may then be written alternatively as

$$\frac{\partial u_n}{\partial t} - c_n\alpha_R^{-1}\frac{\partial T_n}{\partial x} = 0 \tag{12}$$

and

$$\frac{\partial T_n}{\partial t} - c_n\alpha_R\frac{\partial u_n}{\partial x} = Q_n. \tag{13}$$

3) Low-pass filtering of the transformed system

Low-pass filtering in the horizontal (with a cutoff wavelength of 1024 km) serves to isolate the large-scale waves disturbances and also leads to the concept of the convective apparent heat source $Q1$, given by the sum of latent heating plus the heating due to subfilter-scale (i.e., "eddy") fluxes. Heating due to filter-scale fluid motions Qfs completes the picture, but is generally small during the early stages of the simulation when the large-scale waves are first starting to develop (see the appendix for details). With these definitions, and using braces to denote the horizontal filter, (12) and (13) become

$$\frac{\partial\{u_n\}}{\partial t} - c_n\alpha_R^{-1}\frac{\partial\{T_n\}}{\partial x} = 0 \tag{14}$$

and

$$\frac{\partial\{T_n\}}{\partial t} - c_n\alpha_R\frac{\partial\{u_n\}}{\partial x} = \{Q_n\} = Qfs_n + Q1_n. \tag{15}$$

For future reference, we note that (14) and (15) imply the domain-averaged energy conservation relation:

$$\frac{\partial}{\partial t}\left(\underbrace{\frac{\overline{\{u_n\}^2}}{2}}_{\text{KE}_n} + \underbrace{\alpha_R^{-2}\frac{\overline{\{T_n\}^2}}{2}}_{\text{PE}_n}\right) = Sfs_n + S1_n \tag{16}$$

where overbars denote a horizontal domain average. Here, KE_n and PE_n are the large-scale components of the domain-averaged kinetic and available potential energies, respectively, while Sfs_n and $S1_n$ are source terms due to filter-scale and apparent heating, respectively. The source terms are given by

$$Sfs_n = \overline{\alpha_R^{-2}Qfs1_n\{T_n\}} \tag{17a}$$

and

$$S1_n = \overline{\alpha_R^{-2}Q1_n\{T_n\}}, \tag{17b}$$

respectively, which imply that energy is generated (destroyed) when heating and temperature are positively (negatively) correlated with one another. Since the initial wave development process occurs mainly though $Q1_n$ processes, before large-scale wave motions exert advective tendencies Qfs_n (results not shown), we restrict our attention in this study to the apparent energy source $S1_n$.

6. Vertical-mode analysis

Vertical-mode decomposition can now be used to determine which vertical modes are most energetically active on large spatial scales in the simulation, and how these modes are forced and maintained by shallow convective, deep convective, and stratiform heating processes.

a. Heating spectra

The composite heating profiles in Fig. 5 are expressed spectrally in Fig. 9, as a function of modal propagation speed c_n. The deep convective heating spectrum (solid line) exhibits relatively strong positive forcing at 35 and 45 m s^{-1}, implying deep-tropospheric warming ($L_{zn} \cong 25$ km, corresponding to vertical wavelengths roughly twice the depth of the heating). Deep convection also provides forcing in the range of 16–20 m s^{-1}, but with the negative sign implying low-level cooling ($L_{zn} \cong 10$ km). In Fig. 9b, we see that the negative forcing can be attributed to downdraft cooling in high-based convective columns. The positive forcing of the faster/deeper modes, on the other hand, stems

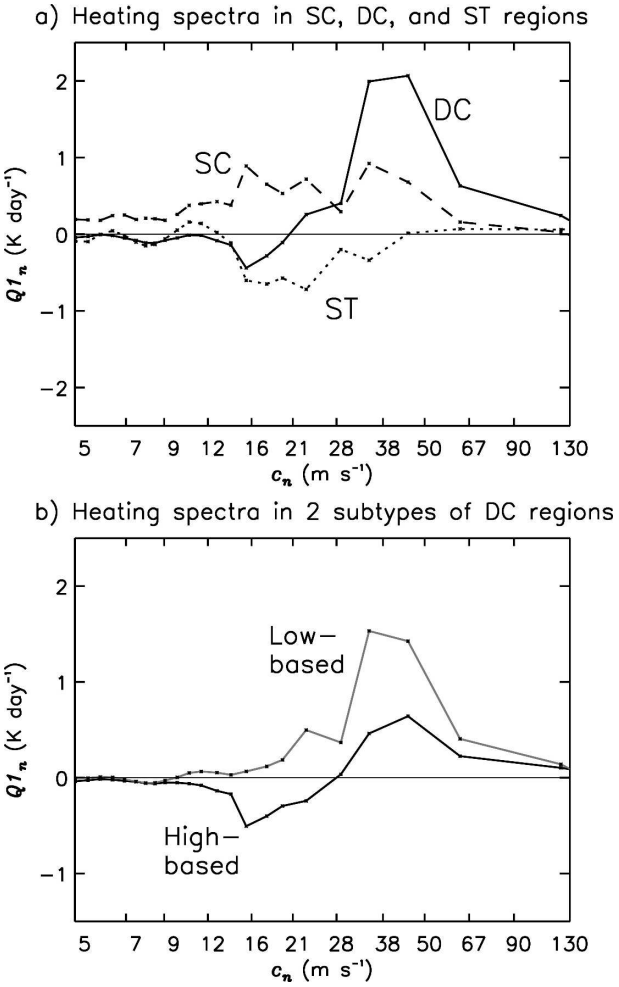

FIG. 9. Spectra of the heating profiles in Fig. 5, expressed as a function mode speed c_n. Because we are mainly interested in the generation of waves in the troposphere, the spectra have been multiplied by the root mean square of ξ_n in the lowest 11 km (so that amplitude is a measure of heating amplitude in this layer).

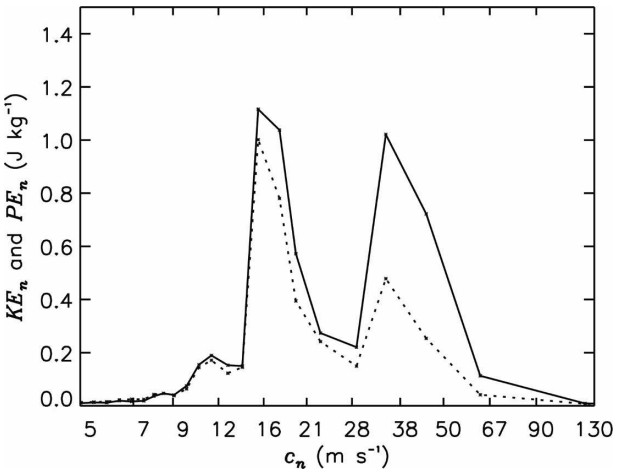

FIG. 10. Spectra of the large-scale kinetic (KE_n) and available potential (PE_n) energies averaged over the entire 15-day simulation.

mainly from low-based deep convective heating, which provides warming through the depth of the troposphere. These spectral forcing components are consistent with the numerical modeling study of Lane and Reeder (2001), who showed that an isolated deep convective cloud excites both a fast-moving ($\sim$50 m s^{-1}) gravity wave response, with deep-tropospheric warming, and a slow-moving ($\sim$16 m s^{-1}) response, with low-level cooling.

The stratiform heating spectrum (dotted curve in Fig. 9a) also exhibits negative forcing in the range 16–20 m s^{-1}, but with additional negative forcing at higher mode speeds (23–45 m s^{-1}). The location of the peak forcing at 23 m s^{-1} can be understood by noting that the negative part of the stratiform heating profile is broadly similar to the temperature structure of this mode below 6 km (cf. Figs. 5a and 8b). Above this level, however, the profile is shallower than the pure 23 m s^{-1} mode profile, resulting in a negative-signed projection onto slower modes (16–20 m s^{-1}). Because the vertical integral of the stratiform heating is negative, the spectrum exhibits a distinct secondary peak at 35 m s^{-1}.

In contrast to the deep convective and stratiform heating spectra, both of which exhibit bands of positive- and negative-signed forcings, the shallow convective spectrum (dashed line in Fig. 9a) is positive at all speeds shown, with a primary peak at 16 m s^{-1} and two slightly lower amplitude peaks at 23 and 35 m s^{-1}. The flatness of the spectrum springs from the fact that the shallow convective heating is highly peaked in physical space. The moderate forcing at 35 and 45 m s^{-1} (comparable to that by high-based deep convective heating, but about 50% smaller than low-based heating) is a consequence of the vertical integral of shallow convective heating being positive.

b. Large-scale wave energetics

Figure 10 identifies which vertical modes are most energetically active in the large-scale wave disturbances, showing time-mean spectra of the large-scale kinetic KE_n and available potential PE_n energies from (16). Despite the broad spectrum of modal excitations seen above, the spectrum of the kinetic energy (solid line) is dominated by just two relatively narrow spectral bands: one with three vertical modes (16, 18, and to a lesser extent 20 m s^{-1}) and another with two modes (35 and 45 m s^{-1}). There is also a weak tertiary band near 12 m s^{-1}. The spectrum of the available potential energy (dotted line) is similar to that of the kinetic energy,

but with substantially lower amplitudes in the faster/deeper (35–67 m s^{-1}) band. These differences arise because deep convective heating anomalies are more or less in phase with convergence anomalies of the fast modes [leading to reduced amplitude of fast-mode temperature anomalies; cf. Gill (1982)] and in quadrature with those of the slow modes [results given in Tulich (2003)].

The apparent energy source $S1_n$ from (16) and (17b) is found to be the dominant source of large-scale wave energy in the simulations, in accordance with previous observational studies by Lau and Lau (1992) and Yanai et al. (2000). As an expansion of this result, Fig. 11a shows how $S1_n$ (averaged over the first 5 days, when the large-scale waves are first becoming organized) is partitioned among shallow convective, deep convective, and stratiform cloud types. To aide the interpretation, we note that a positive (negative) value of $S1_n$ implies a positive (negative) correlation between apparent heating $Q1_n$ and large-scale filtered temperature $\{T_n\}$ anomalies.

Deep convective heating, as indicated by the solid curve, is a source of both fast- and slow-mode energy, as well as a weak sink in the ultraslow (~12 m s^{-1}) band. Separation of this spectrum into high- and low-based components (Fig. 11b) shows that high-based deep convective heating (with $Q1_{\text{slow}} \ll 0$) is essential for driving the slow modes, while the generation of the fast modes stems from both high- and low-based heating (with $Q1_{\text{fast}} \gg 0$). The stratiform spectrum (dotted curve) also exhibits strong production of the slow modes (with amplitude roughly twice that of the deep convective spectrum), but with a tail extending upward past 20 m s^{-1}. Stratiform heating, together with shallow convective heating, also provides a weak source of energy in the ultraslow band. At higher mode speeds (16–23 m s^{-1}), however, shallow convective heating provides a strong sink that is comparable to the source from stratiform heating. Thus, while deep convective and stratiform heating both play a positive role in the generation of large-scale wave energy, shallow convective heating plays mainly a destructive role.

c. Vertical-mode truncation of the large-scale wave structures

As might be expected on the basis of the energy spectra in Fig. 10, much of the tilted structure of the waves can be captured by just two spectral "bands" (here, pairs of vertical modes): a pair of "fast" modes with $c_n \cong 35$ and 45 m s^{-1} ($L_{zn} \cong 21$ and 27 km) and a pair of "slow" modes with $c_n \cong 16$ and 18 m s^{-1} ($L_{zn} \cong 9$ and 11 km). This is illustrated in Fig. 12 (top two panels), which show vertically truncated versions of the composite distributions of temperature and horizontal wind anomalies in Fig. 2. Overall, we see that the truncated wave structures capture much of the full wave structures discussed earlier in section 4a. The truncated structures are a bit "blocky" with some sharp tilts missing, especially in the case of the temperature anomaly field. Also, the finescale structures of the waves in the boundary layer are not captured by the truncated system (cf. Haertel and Kiladis 2004).

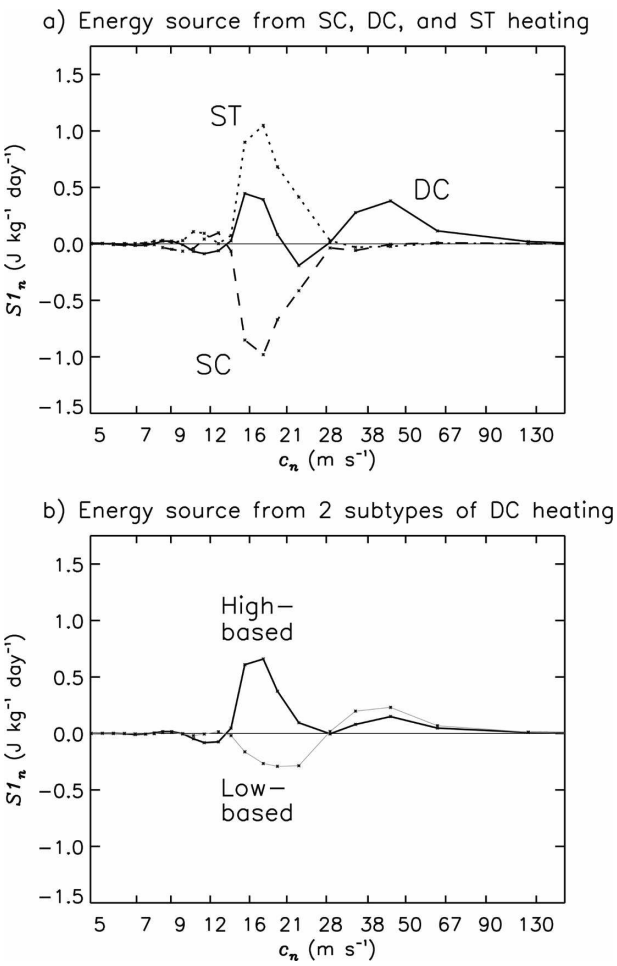

FIG. 11. Cloud-partitioned spectra of the apparent energy source $S1_n$ from (16) and (17b), averaged over the first 5 days of the simulation.

The bottom two panels in Fig. 12 show the improvements gained by retaining two additional ("ultraslow") modes in the truncation: the 11 and 12 m s^{-1} modes, corresponding to tropospheric wavelengths in the range 6–7 km. Comparing Figs. 11c and 2a, we see that the low-level "wedge" structure of temperature anomalies (e.g., cool near 3000 km and warm near 5000 km) is just starting to be resolved by the truncated system with three spectral bands. If this low-level structure is important to the modulation of convective development

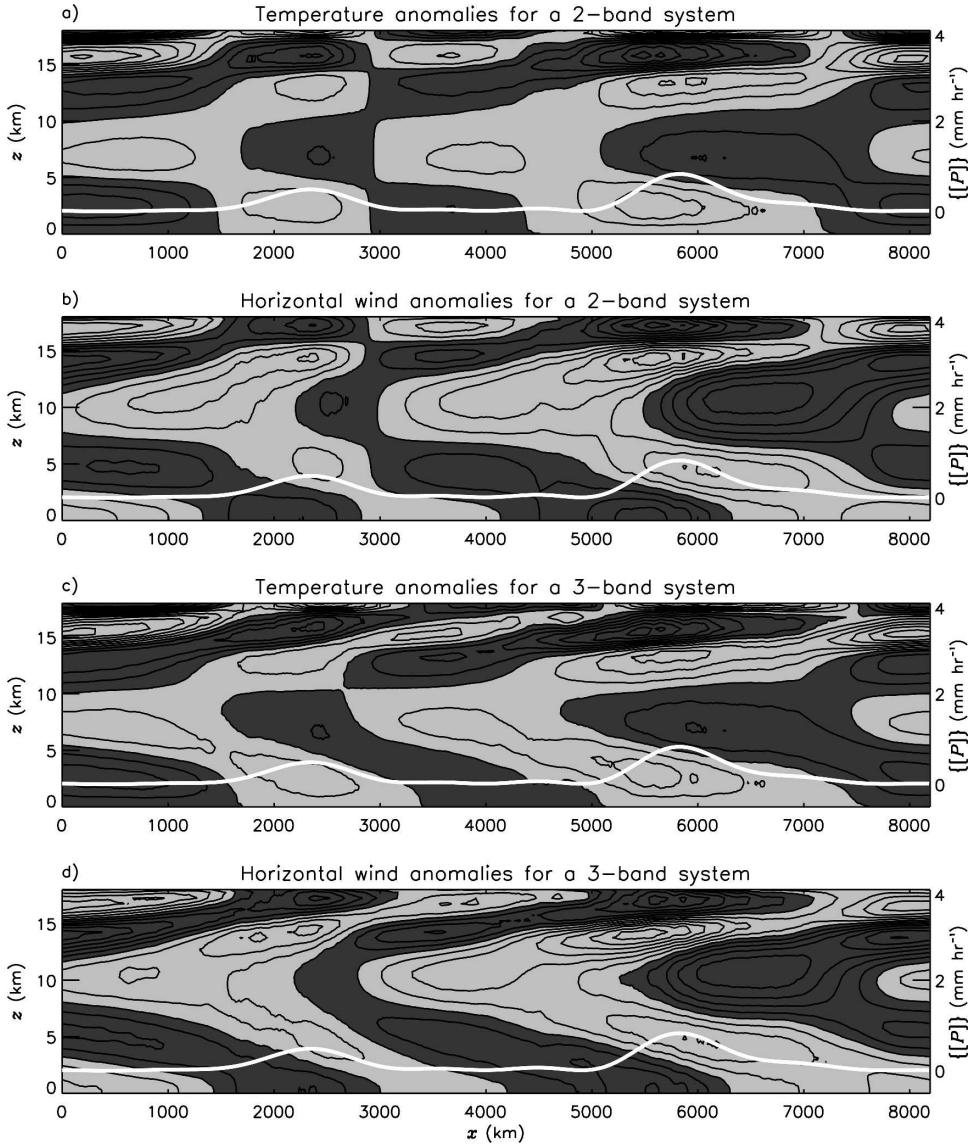

FIG. 12. Similar to the upper two panels in Fig. 2 but with vertical resolution truncated to include only (a), (b) the "fast" and "slow" modes or (c), (d) the fast, slow, and "ultraslow" (11 and 12 m s^{-1}) modes. See text for details.

(as suggested by Figs. 4 and 6), then tropical wave models with only two modes of vertical structure (e.g., Mapes 2000; Majda and Shefter 2001) may incur significant errors in low-level convection modulation. The improvements in the stratosphere also indicate that the inclusion of these higher-order modes is essential for capturing the upward propagation of wave energy in the stratosphere.

d. Sensitivity study

The discussion thus far has focused on large-scale cloud disturbances produced spontaneously under uniform radiative cooling (of depth ~12 km) and a uniform SST of 300 K. To assess the model's sensitivity to these choices, we performed two additional simulations, each having a slightly different model setup. The setup for the first simulation (referred to as DEEP) is similar to that of the standard run except that the pressure level at which the radiative cooling decays linearly to zero is decreased from 200 to 125 mb, resulting in a ~2.5 km increase in the depth of the cooling (not shown). The second simulation (referred to as WARM) is similar to the DEEP simulation, except that the SST is also increased from 300 to 303 K, resulting in both a

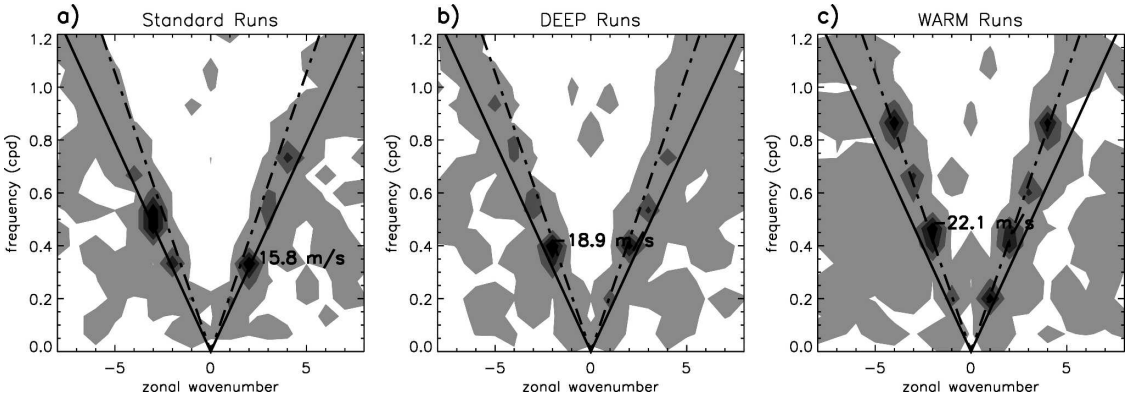

FIG. 13. Ensemble-averaged, space–time (Fourier) spectra of the surface precipitation rate P in the (a) standard, (b) DEEP, and (c) WARM simulations. Solid and dashed lines denote gravity wave speeds of 15 and 20 m s^{-1}, with positive (negative) wavenumbers corresponding to rightward- (leftward-) moving signals. For ease of comparison, phase speeds associated with the peaks in each spectra have been indicated.

warmer and wetter troposphere. To increase the statistical robustness of the results, both simulations were repeated five times using slightly different initial conditions.

As in Fig. 1, both simulations exhibit spontaneous development of large-scale convectively coupled wave disturbances. Comparing the space–time spectra of surface precipitation P in Fig. 13, however, we see that the propagation speeds of the waves in the DEEP simulations are about 20% (~3 m s^{-1}) larger than in the standard simulations, while those in the WARM simulations are about 40% (~6 m s^{-1}) larger. While more detailed analyses are ultimately needed to explain this behavior, Fig. 14 shows that the changes in wave speed are accompanied by corresponding shifts in the peaks of the large-scale wave energy spectra, which in turn can be related to changes in the spectral properties of the background cooling (see Fig. 15). Such consistency among theoretically predicted mode speeds c_n and objectively determined wave speeds is encouraging and provides some evidence to suggest that the propagation speed of the large-scale waves is set by the "dry" speed of the slow modes. The alternative hypothesis of a reduced-stability, fast-mode mechanism of wave propagation (e.g., Gill 1982; Emanuel et al. 1994), however, cannot be ruled out.

7. Summary and discussion

This paper demonstrated that spontaneous development of large-scale wave disturbances in 2D simulations of radiative–convective equilibrium can be fruitfully analyzed in the simplified discrete space of three cloud types and two main vertical spectral "bands." Both the convection and wave circulation patterns have structures broadly resembling those of observed convectively coupled Kelvin waves (e.g., Wheeler et al. 2000; Straub and Kiladis 2003), so the results may be realistic enough to bear on this type of phenomenon. The diagnosed energetics of upscale wave development appear to have reasonable sources and sinks, with deep convective and stratiform heating both playing a positive role in wave growth and shallow convective heating playing a negative role. This part of the coupled phenomenon (wave driving by convection) has long been seen as the easier half to understand at a diagnostic level, though the importance of deep convective heat-

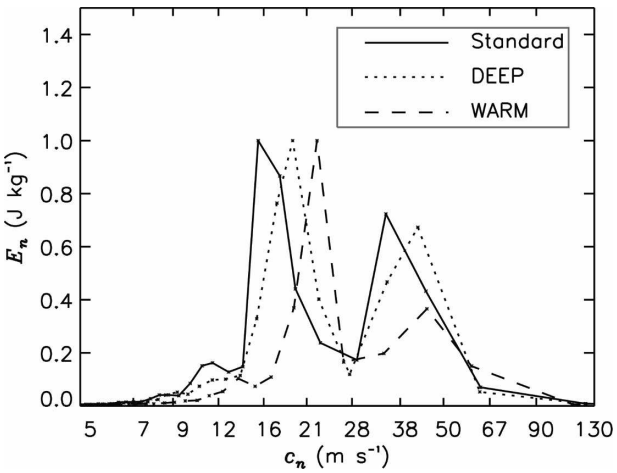

FIG. 14. Ensemble-averaged spectra of the time-mean large-scale wave energy E_n (given by the sum of KE$_n$ and PE$_n$) in the standard (solid), DEEP (dotted), and WARM (dashed) simulations. For ease of comparison, each spectra has been normalized by its peak amplitude. Spectra for the DEEP and WARM simulations were computed using the set of vertical modes associated with their respective time-mean soundings.

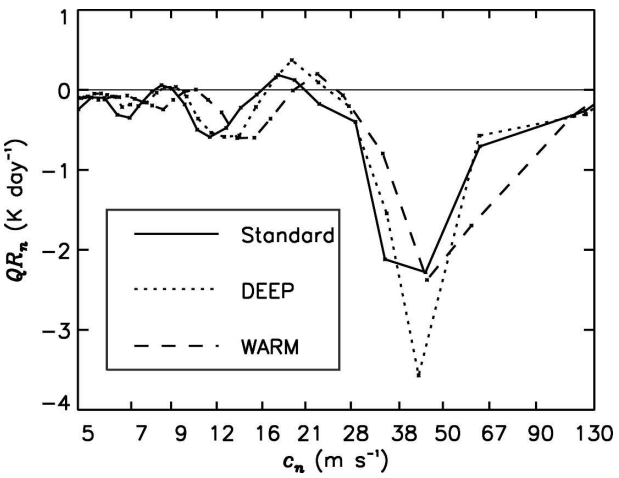

FIG. 15. Spectra of imposed radiative cooling QR_n in the standard (solid), DEEP (dotted), and WARM (dashed) simulations. Spectra for the DEEP and WARM simulations were computed using the set of vertical modes associated with their respective time-mean soundings. As in Fig. 11, the spectra have been multiplied by the root mean square of ξ_n in the lowest 11 km.

ing in shallow-wave driving has not been widely recognized.

The tools outlined here may be useful for characterizing and understanding the harder half of the coupled phenomenon: wave modulation of convection. One fruitful approach is to examine more closely the initial growth stage of the waves (days 1–5), with a view toward isolating the key mechanisms involved. A companion paper that addresses this issue from both a Fourier perspective (growth of large-scale wave components) and a contiguous-region perspective (merger of narrow wet and dry zones into larger ones) is currently in preparation.

Another approach for isolating key mechanisms is through running model sensitivity experiments. Section 6e illustrated how such experiments can be used to address questions about which vertical modes are most active and how the structures of these modes relate to large-scale wave propagation speed. More definitive and detailed conclusions may be reachable though further analysis and experimentation. The goal is to tease apart the effects of stability, cloud depth, and moisture via simple changes in global parameters.

In summary, the decomposition methods described in this paper provide a useful framework for raising and addressing scientific questions, of importance to large-scale weather and climate modeling. It is hoped that further diagnoses in this vein will begin to answer some of these questions more robustly.

Acknowledgments. We thank Dr. Marat Khairoutdinov, for his assistance in running and modifying the CSU SAM, and Dr. Scott Fulton, for providing his vertical normal mode transform algorithm. The assistance of Lyle Pakula in using the supercomputers at the Scientific Computing Division of the National Center for Atmospheric Research, where the model simulations were performed, is also greatly appreciated. Numerous discussions with Prof. Wayne Schubert helped to inspire this work. Comments by Dr. Todd Lane and an anonymous reviewer lead to improvements in an earlier version of this manuscript. Funding for this research was provided by the National Science Foundation under Grants ATM-9812384 and ATM-0555570.

APPENDIX

Definition of the Convective Apparent Heat Source

This appendix describes our method used to define the convective apparent heat source, appropriate to the context of a low-pass–filtered large-scale wave.

All fields are separated into large- and small-scale components, where the former are obtained using a low-pass Lanczos filter with a cutoff wavelength of 1024 km (denoted by $\{\cdot\}$) and the latter are obtained as a residual; that is,

$$u' = u - \{u\}. \tag{A1}$$

Recognizing that the product of any two fields can be expanded as

$$uT = \{u\}\{T\} + u'\{T\} + \{u\}T' + u'T', \tag{A2}$$

we write the governing equation for "large-scale" temperature anomalies as

$$\frac{\partial\{T\}}{\partial t} + \frac{1}{\rho_s}\nabla\cdot(\rho_s\{\{\mathbf{u}\}\{T\}\}) + \{w\}\frac{\overline{T}\,\overline{N}^2}{g} = Q1, \tag{A3}$$

where ρ_s is the basic-state density, $\mathbf{u}$ is the velocity vector, $\nabla\cdot(\cdot)$ is the divergence operator, $\overline{T}$ is the domain-averaged temperature, $\overline{N}$ is the domain-averaged Brunt–Väisälä frequency, and $Q1$ is the convective apparent heat source, defined as

$$Q1 \equiv \{Q_{\text{mic}}\} - \frac{1}{\rho_s}\nabla\cdot(\rho_s(\{\mathbf{u}'\{T\}\} + \{\{\mathbf{u}\}T'\} + \{\mathbf{u}'T'\})), \tag{A4}$$

where Q_{mic} is the temperature tendency due to phase changes of water substance, while the remaining terms represent the temperature tendency due to subfilter-scale (but model resolved) divergences of sensible heat fluxes. Note: the tendency due to the spatially uniform

radiative cooling is neglected since it provides no source of horizontal temperature variance. Also, the tendency due to the parameterized flux is neglected for simplicity. In other words, the convective apparent heat source $Q1$ represents the large-scale component of latent heating plus the heating due to "eddy"-flux divergences. This definition is similar to the conventional definition of Yanai et al. (1973), except that the Reynolds conditions and their consequences are not assumed; that is, the cross terms $\{\mathbf{u}'\{T\}\}$ and $\{\{\mathbf{u}\}T'\}$ are retained.

With this definition, the total large-scale heating $\{Q\}$ can be defined as

$$\{Q\} \equiv Qfs + Q1, \tag{A5}$$

where

$$Qfs \equiv -\frac{1}{\rho_s}\nabla \cdot (\rho_s\{\{\mathbf{u}\}\{T\}\}) \tag{A6}$$

represents the heating due to transports of filter-scale temperature anomalies by filter-scale wave motions. For completeness, we note that this "resolved" heating component is negligible during the growth stage of the large-scale waves, but provides an important sink of energy during their mature stage (results not shown).

REFERENCES

Caniaux, G., J.-L. Redelsperger, and J.-P. Lafore, 1994: A numerical study of the stratiform region of a fast-moving squall line. Part I: General description and water and heat budgets. *J. Atmos. Sci.,* **51,** 2046–2074.

Chang, C.-P., and H. Lim, 1988: Kelvin wave-CISK: A possible mechanism for the 30–50 day oscillations. *J. Atmos. Sci.,* **45,** 1709–1720.

Chao, W. C., and S.-J. Lin, 1994: Tropical intraseasonal oscillation, super cloud clusters, and cumulus convection schemes. *J. Atmos. Sci.,* **51,** 1282–1297.

Crum, F. X., and D. E. Stevens, 1983: A comparison of two cumulus parameterization schemes in a linear model of wave-CISK. *J. Atmos. Sci.,* **40,** 2671–2688.

Davies, H. C., 1979: Phase-lagged wave-CISK. *Quart. J. Roy. Meteor. Soc.,* **105,** 325–353.

Emanuel, K. A., J. D. Neelin, and C. S. Bretherton, 1994: On large-scale circulations in convective atmospheres. *Quart. J. Roy. Meteor. Soc.,* **120,** 1111–1143.

Fulton, S. R., and W. H. Schubert, 1985: Vertical normal transforms: Theory and application. *Mon. Wea. Rev.,* **113,** 647–658.

Gill, A. E., 1982: Studies of moisture effects in simple atmospheric models: The stable case. *Geophys. Astrophys. Fluid Dyn.,* **19,** 119–152.

Goswami, P., and B. N. Goswami, 1991: Modification of $n = 0$ equatorial waves due to interaction between convection and dynamics. *J. Atmos. Sci.,* **48,** 2231–2244.

Grabowski, W. W., 2003: Impact of ice microphysics on multiscale organization of tropical convection in two-dimensional cloud resolving model simulations. *Quart. J. Roy. Meteor. Soc.,* **129,** 67–81.

——, and M. W. Moncrieff, 2001: Large-scale organization of tropical deep convection in two-dimensional explicit numerical simulations. *Quart. J. Roy. Meteor. Soc.,* **127,** 445–468.

——, J.-I. Yano, and M. W. Moncrieff, 2000: Cloud resolving modeling of tropical circulations driven by large-scale SST gradients. *J. Atmos. Sci.,* **57,** 2022–2040.

Haertel, P. T., and R. H. Johnson, 1998: Two-day disturbances in the equatorial western Pacific. *Quart. J. Roy. Meteor. Soc.,* **124,** 615–636.

——, and G. K. Kiladis, 2004: Dynamics of 2-day equatorial waves. *J. Atmos. Sci.,* **61,** 2707–2721.

Hayashi, Y., 1970: A theory of large-scale equatorial waves generated by condensation heat and accelerating the zonal wind. *J. Meteor. Soc. Japan,* **48,** 140–160.

Houze, R. A., Jr., 1977: Structure and dynamics of a tropical squall line system. *Mon. Wea. Rev.,* **105,** 1540–1567.

——, 1982: Cloud clusters and large-scale vertical motions in the tropics. *J. Meteor. Soc. Japan,* **60,** 396–410.

——, 1989: Observed structure of mesoscale convective systems and implications for large-scale heating. *Quart. J. Roy. Meteor. Soc.,* **115,** 425–461.

——, 1997: Stratiform precipitation in regions of convection: A meteorological paradox? *Bull. Amer. Meteor. Soc.,* **78,** 2179–2196.

Johnson, R. H., and G. S. Young, 1983: Heat and moisture budgets of tropical mesoscale anvil clouds. *J. Atmos. Sci.,* **40,** 2138–2147.

Kasahara, A., and K. Puri, 1981: Spectral representation of three-dimensional global data by expansion in normal mode functions. *Mon. Wea. Rev.,* **109,** 37–51.

Khairoutdinov, M. F., and D. A. Randall, 2003: Cloud-resolving modeling of the ARM summer 1997 IOP: Model formulation, results, uncertainties, and sensitivities. *J. Atmos. Sci.,* **60,** 607–625.

Khouider, B., and A. J. Majda, 2006: A simple multicloud parameterization for convectively coupled tropical waves. Part I: Linear analysis. *J. Atmos. Sci.,* **63,** 1308–1323.

Kuang, Z., P. N. Blossey, and C. S. Bretherton, 2005: A new approach for 3D cloud resolving simulations of large scale atmospheric circulation. *Geophys. Res. Lett.,* **32,** L02809, doi:10.1029/2004GL021024.

Lane, T. P., and M. J. Reeder, 2001: Convectively generated gravity waves and their effect on the cloud environment. *J. Atmos. Sci.,* **58,** 2427–2440.

Lang, S., W.-K. Tao, J. Simpson, and B. Ferrier, 2003: Modeling of convective–stratiform precipitation processes: Sensitivity to partitioning methods. *J. Appl. Meteor.,* **42,** 505–527.

Lau, K.-H., and N.-C. Lau, 1992: The energetics and propagation dynamics of tropical summertime synoptic-scale disturbances. *Mon. Wea. Rev.,* **120,** 2523–2539.

Lin, J. W.-B., and J. D. Neelin, 2002: Considerations for stochastic convective parameterization. *J. Atmos. Sci.,* **59,** 959–975.

Lindzen, R. S., 2003: The interaction of waves and convection in the Tropics. *J. Atmos. Sci.,* **60,** 3009–3020.

Majda, A. J., and M. G. Shefter, 2001: Models for stratiform instability and convectively coupled waves. *J. Atmos. Sci.,* **58,** 1515–1535.

Mapes, B. E., 1998: The large-scale part of tropical mesoscale convective circulations: A linear vertical spectral band model. *J. Meteor. Soc. Japan,* **76,** 29–55.

——, 2000: Convective inhibition, subgrid-scale triggering energy, and stratiform instability in a toy tropical wave model. *J. Atmos. Sci.,* **57,** 1515–1535.

——, and R. A. Houze Jr., 1992: An integrated view of the 1987 Australian monsoon and its mesoscale convective systems. Part I: Horizontal structure. *Quart. J. Roy. Meteor. Soc.,* **118,** 927–963.

——, and ——, 1995: Diabatic divergence profiles in tropical mesoscale convective systems. *J. Atmos. Sci.,* **52,** 1807–1828.

——, S. N. Tulich, J.-L. Lin, and P. Zuidema, 2006: The mesoscale convection life cycle: Building block or prototype for large-scale tropical waves? *Dyn. Atmos. Oceans,* **42,** 3–29.

Nakazawa, T., 1988: Tropical super clusters within intraseasonal variations over the western Pacific. *J. Meteor. Soc. Japan,* **66,** 777–786.

Oouchi, K., 1999: Hierarchical organization of super cloud clusters caused by WISHE, convectively induced gravity waves and cold pool. *J. Meteor. Soc. Japan,* **77,** 907–927.

——, and M. Yamasaki, 2002: An MJO-like gravity wave and superclusters simulated in a two-dimensional cumulus-scale-resolving model under a warm pool condition. *J. Meteor. Soc. Japan,* **79,** 201–218.

Peng, L., C.-H. Sui, K.-M. Lau, and W.-K. Tao, 2001: Genesis and evolution of hierarchical cloud clusters in a two-dimensional cumulus-resolving model. *J. Atmos. Sci.,* **58,** 877–895.

Roundy, P. E., and W. M. Frank, 2004: A climatology of waves in the equatorial region. *J. Atmos. Sci.,* **61,** 2105–2132.

Stark, T. E., 1976: Wave-CISK and cumulus parameterization. *J. Atmos. Sci.,* **33,** 2383–2391.

Straub, K. H., and G. N. Kiladis, 2002: Observations of convectively coupled Kelvin waves in the eastern Pacific ITCZ. *J. Atmos. Sci.,* **59,** 30–53.

——, and ——, 2003: The observed structure of convectively coupled Kelvin waves: Comparison with simple models of coupled wave instability. *J. Atmos. Sci.,* **60,** 1655–1668.

Su, H., C. S. Bretherton, and S. S. Chen, 2000: Self-aggregation and large-scale control of tropical deep convection: A modeling study. *J. Atmos. Sci.,* **57,** 1797–1816.

Takayabu, Y. N., 1994: Large-scale cloud disturbances associated with equatorial waves. Part I: Spectral features of the cloud disturbances. *J. Meteor. Soc. Japan,* **72,** 433–448.

——, and M. Murakami, 1991: The structure of super cloud clusters observed in 1–20 June 1986 and their relationship to easterly waves. *J. Meteor. Soc. Japan,* **69,** 105–125.

——, K.-M. Lau, and C.-H. Sui, 1996: Observation of a quasi-2-day wave during TOGA COARE. *Mon. Wea. Rev.,* **124,** 1892–1913.

Tao, W.-K., and J. Simpson, 1989: Modeling study of a tropical squall-type convective line. *J. Atmos. Sci.,* **46,** 177–202.

——, S. Lang, J. Simpson, and R. Adler, 1993: Retrieval algorithms for estimating the vertical profiles of latent heat release: Their applications for TRMM. *J. Meteor. Soc. Japan,* **71,** 685–700.

Tomita, H., H. Miura, S. Iga, T. Nasuno, and M. Satoh, 2005: A global cloud-resolving simulation: Preliminary results from an aqua planet experiment. *Geophys. Res. Lett.,* **32,** L08805, doi:10.1029/2005GL022459.

Tulich, S. N., 2003: On the interactions between tropical convection and gravity waves: Comparisons between simple models and simulations. Ph.D. thesis, Colorado State University, Fort Collins, CO, 153 pp.

Wheeler, M., and G. N. Kiladis, 1999: Convectively coupled equatorial waves: Analysis of clouds and temperature in the wavenumber–frequency domain. *J. Atmos. Sci.,* **56,** 374–399.

——, and K. M. Weickmann, 2001: Real-time monitoring of modes of coherent synoptic to intraseasonal variability. *Mon. Wea. Rev.,* **129,** 2677–2694.

——, G. N. Kiladis, and P. J. Webster, 2000: Large-scale dynamical fields associated with convectively coupled equatorial waves. *J. Atmos. Sci.,* **57,** 613–639.

Wu, Z., 2003: A shallow CISK, deep equilibrium mechanism for the interaction between large-scale convection and large-scale circulations in the Tropics. *J. Atmos. Sci.,* **60,** 377–392.

Xu, K.-M., 1995: Partitioning mass, heat, and moisture budgets of explicitly simulated cumulus ensembles into convective and stratiform components. *J. Atmos. Sci.,* **52,** 551–573.

Yanai, M., S. Esbensen, and J.-H. Chu, 1973: Determination of bulk properties of tropical cloud clusters from large-scale heat and moisture budgets. *J. Atmos. Sci.,* **30,** 611–627.

——, B. Chen, and W.-W. Tung, 2000: The Madden–Julian oscillation observed during the TOGA COARE IOP: Global view. *J. Atmos. Sci.,* **57,** 2374–2396.

Yang, G.-Y., B. Hoskins, and J. Slingo, 2003: Convectively coupled equatorial waves: A new methodology for identifying wave structures in observational data. *J. Atmos. Sci.,* **61,** 1637–1654.

Yano, J.-I., J. C. McWilliams, M. W. Moncrieff, and K. A. Emanuel, 1995: Hierarchical tropical cloud systems in an analog shallow-water model. *J. Atmos. Sci.,* **52,** 1723–1742.

Zipser, E. J., 1977: Mesoscale and convective-scale downdrafts as distinct components of squall-line structure. *Mon. Wea. Rev.,* **105,** 1568–1589.

——, R. J. Meitlen, and M. A. LeMone, 1981: Mesoscale motion field associated with a slowly moving GATE convective band. *J. Atmos. Sci.,* **38,** 1725–1750.